ELSEVIER

Multiscale finite-volume method for compressible multiphase flow in porous media

Ivan Lunati [*], Patrick Jenny

Institute of Fluid Dynamics, ETH Zürich, 8092 Zürich, Switzerland

Abstract

The Multiscale Finite-Volume (MSFV) method has been recently developed and tested for multiphase-flow problems with simplified physics (i.e. incompressible flow without gravity and capillary effects) and proved robust, accurate and efficient. However, applications to practical problems necessitate extensions that enable the method to deal with more complex processes. In this paper we present a modified version of the MSFV algorithm that provides a suitable and natural framework to include additional physics. The algorithm consists of four main steps: computation of the local basis functions, which are used to extract the coarse-scale effective transmissibilities; solution of the coarse-scale pressure equation; reconstruction of conservative fine-scale fluxes; and solution of the transport equations. Within this framework, we develop a MSFV method for compressible multiphase flow. The basic idea is to compute the basis functions as in the case of incompressible flow such that they remain independent of the pressure. The effects of compressibility are taken into account in the solution of the coarse-scale pressure equation and, if necessary, in the reconstruction of the fine-scale fluxes. We consider three models with an increasing level of complexity in the flux reconstruction and test them for highly compressible flows (tracer transport in gas flow, imbibition and drainage of partially saturated reservoirs, depletion of gas–water reservoirs, and flooding of oil–gas reservoirs). We demonstrate that the MSFV method provides accurate solutions for compressible multiphase flow problems. Whereas slightly compressible flows can be treated with a very simple model, a more sophisticate flux reconstruction is needed to obtain accurate fine-scale saturation fields in highly compressible flows.
© 2006 Elsevier Inc. All rights reserved.

Keywords: Compressibility; Multiscale methods; Finite-volume methods; Multiphase flow in porous media; Reservoir simulation

1. Introduction

Important human activities such as sustainable management of water resources and optimal exploitation of oil reservoirs presuppose a deep understanding of flow in porous media, which makes it possible to develop reliable tools to simulate and predict the response of systems under different flow scenarios. When dealing with large porous media such as subsurface reservoirs, one of the most challenging problems is the dramatic spatial

---
[*] Corresponding author. Tel.: +41 44 632 0917; fax: +41 44 632 1147.
E-mail addresses: lunati@ifd.mavt.ethz.ch (I. Lunati), jenny@ifd.mavt.ethz.ch (P. Jenny).

variability of medium properties such as hydraulic permeability. The latter typically displays complex correlation structures that span a wide range of scales [8,6]. Most important, the small-scale heterogeneity affects flow and transport at much larger scales and has an impact on the macroscopic response of the reservoir. The importance of fine-scale effects has been widely recognized and has led toward higher-resolution techniques for reservoir characterization. Nowadays, high-resolution permeability fields consisting of many million cells can be obtained, e.g. by geostatistical techniques or geological models. The computational costs of numerical simulations—which often include investigation of different flow scenarios or Monte Carlo simulations involving hundreds of realizations of equally probable permeability fields—soon become prohibitive.

To increase efficiency, a variety of upscaling techniques to coarsen the permeability models have been developed over the last three decades (see [13] or [14] for a comprehensive review). The common idea to all these methods is to replace a heterogeneous medium by a homogeneous medium characterized by an equivalent (or effective) permeability, which correctly reproduces the large-scale evolution of some quantity of interest (e.g. pressure, flux, energy dissipation). Even though these methods can be successfully employed for a variety of problems, they might fail when applied to fields displaying complex non-stationary correlation structures. Moreover, as the definition of equivalent permeability is not unique, but depends on the observation variable of interest, extension to real problems governed by nonlinear equations and involving many physical processes (such as reactive transport or multiphase flow) is problematic. The loss of information introduced by coarsening together with the lack of realistic assumptions about the small-scale distribution of the system variables will result in inaccurate predictions of the large scale behavior.

To overcome these problems a flourishing activity on multiscale modeling of oil reservoirs has developed. In contrast to upscaling, the focus here is not only to capture the large-scale behavior of the system, but to solve the problem with the original resolution. The goal is to be as accurate as fine-sale simulations keeping the computational costs comparable with traditional upscaling methods. In recent years several promising advances have been made in this area. All methods employ fine and coarse computational grids and deal with a pressure-saturation formulation of multiphase flow. The latter involves the solution of an elliptic/parabolic flow equation for the pressure and hyperbolic transport equations for the saturations. These equations are highly nonlinear and tightly coupled.

Gautier et al. [7] describe an approach for fast simulation of flow and transport in heterogeneous media. They use nested grids to construct the fine-scale flow field, then they integrate the saturation equation along the streamlines to solve the transport problem. Hou and Wu [9] present a multiscale finite-element method. They construct basis functions that are specifically designed to capture the fine-heterogeneity. Localization is achieved by assuming ad hoc boundary condition at the coarse element interfaces. In order to reduce the influence of local boundary conditions, an over-sampling technique is employed. In general, however, the reconstructed fine-scale velocity field is not conservative. Later, Chen and Hou [4] propose a conservative mixed finite-element multiscale method. They provide clear evidence that a locally conservative fine-scale velocity field is a necessary requirement for accurate modeling of fluid transport. Arbogast [2] and Arbogast and Bryant [3] present another mixed finite-element multiscale approach for two-phase flow in heterogeneous media. Again, localization is achieved by special boundary conditions at the coarse-element boundaries. The fine-scale influence is then coupled with the coarse-scale effects by means of numerical Greens functions. A mixed multiscale finite element that resembles the one by Chen and Hou is proposed by Aarnes et al. [1] who use it together with a streamline method to solve the saturation equation. Recently, Jenny et al. [10,11] presented a multiscale finite-volume (MSFV) method. They use two sets of basis functions to solve the elliptic problem efficiently and then they compute a locally conservative velocity field. Comparison with an established finite-volume simulator demonstrated the excellent performance of the MSFV algorithm in terms of both accuracy and efficiency. In contrast to other multiscale methods, the MSFV method is based on a finite-volume discretization and therefore has technical and practical advantages for industrial oil-reservoir simulation. Indeed, a mass conservative velocity field is obtained by solving a mass balance equation, which, we believe, facilitates incorporating more complex physics. Moreover, it follows the main-stream of the currently established simulators in reservoir engineering, which are based on finite-volume discretization. This fact increases the appeal of the method for industrial and practical applications.

All the methods above deal with single- or two-phase flow and only consider very simplified physics. They neglect capillary pressure, gravity, and dissolution. They also assume that both the porous medium and the

fluids are incompressible. In this paper we explain how the last two assumptions can be relaxed in the framework of the MSFV method while maintaining the advantages in terms of efficiency. This is made possible by a major change in the original MSFV algorithm that increases computational efficiency for most cases and simplifies the incorporation of additional physical processes.

2. Governing equations

In this paper we consider the flow of m compressible phases in a porous medium, such that we have a system of m partial differential transport equations of the form

$$\frac{\partial}{\partial t}(\phi b_\alpha S_\alpha) + \nabla \cdot (b_\alpha \boldsymbol{u}_\alpha) = -b_\alpha q_\alpha, \tag{1}$$

where $\alpha = 1, \ldots, m$ denotes the phase. The coefficient b_α characterizes the α-phase compressibility and is a function of the pressure p. It can be regarded either as the phase density or as the inverse of the α-phase formation-volume factor, $B_\alpha = 1/b_\alpha$, which is an engineering quantity widely used in the oil industry. B_α is defined as the ratio of the volume occupied by a fixed mass of the fluid at reservoir conditions to the volume occupied at standard conditions. Porosity, ϕ, may also be a function of pressure for elastic porous media. If we neglect capillary pressure and gravity, the Darcy velocity (specific flux) of the α-phase is

$$\boldsymbol{u}_\alpha = -\frac{k_{r\alpha}}{\mu_\alpha}\mathbf{k} \cdot \nabla p, \tag{2}$$

where $\mathbf{k}$ is the absolute permeability tensor, k_{r_α} the relative permeability and μ_α the viscosity of the α-phase. In the following, we will refer to the Darcy velocity simply as "velocity", keeping in mind that Eq. (2) actually represents a volumetric flux per unit area and not the real velocity of the α-phase in the pore (the latter is obtained dividing the Darcy velocity by the porosity). The volumetric source terms, q_α, and the relative permeabilities, $k_{r\alpha}$, are functions of saturation, whereas the viscosities, μ_α, are assumed to be constant. Eq. (1) are solved for pressure, p, and phase saturations, S_α, on a domain Ω with some boundary conditions at $\partial\Omega$. Introducing the constitutive relationships, $b_\alpha(p)$ and $\phi(p)$, and the relative permeability–saturation relationships, $k_{r\alpha}(S_\alpha)$, one obtains a closed system consisting of the m nonlinear partial-differential equation (1), and the constraint

$$\sum_{\alpha=1}^{m} S_\alpha \equiv 1. \tag{3}$$

An equivalent mathematical formulation that is widely used due to several numerical advantages is the pressure-saturation formulation. In this formulation, the primary variables are the pressure and the saturations of $m - 1$ phases. Eq. (3) is used to eliminate the mth saturation. The set of partial differential equations, Eq. (1), is manipulated to obtain an equation for the pressure and $m - 1$ transport equations for the phase saturations. To obtain the pressure equation, Eq. (1) are divided by b_α and added. After a few elementary manipulations one obtains

$$\nabla \cdot (\boldsymbol{\lambda} \cdot \nabla p) = q + \frac{\partial \phi}{\partial t} + \sum_{\alpha=1}^{m} \phi S_\alpha \frac{\partial \ln b_\alpha}{\partial t} - \sum_{\alpha=1}^{m} [(\boldsymbol{\lambda}_\alpha \cdot \nabla p) \cdot \nabla \ln b_\alpha], \tag{4}$$

where $q = \sum_{\alpha=1}^{m} q_\alpha$ is the total volumetric-source term, $\boldsymbol{\lambda}_\alpha = \mathbf{k} k_{r\alpha}/\mu_\alpha$ are the α-phase mobility tensors, and $\boldsymbol{\lambda} = \sum_{\alpha=1}^{m} \boldsymbol{\lambda}_\alpha$ is the total-mobility tensor. The $m - 1$ transport equations have the same form as Eq. (1) and are hyperbolic. Eq. (4) is in general parabolic because ϕ and b_α are functions of p.

3. Multiscale finite-volume method for incompressible flow

For incompressible fluids and rigid porous media, the last three terms on the r.h.s. of Eq. (4) become zero and the equation degenerates into the elliptic equation

$$\nabla \cdot (\boldsymbol{\lambda} \cdot \nabla p) = q \quad \text{on } \Omega. \tag{5}$$

To solve this type of equations efficiently in highly heterogeneous porous media, Jenny et al. [10] proposed the MSFV algorithm. An auxiliary coarse grid is imposed and together with its dual grid it is used to solve the problem (Fig. 1). Two sets of basis functions are used: the first to find the effective parameters for the coarse problem, the second set to reconstruct a velocity field with the same resolution as the original problem. The latter is determined by the resolution of the permeability-field heterogeneity, which can be much finer than the imposed coarse grid. The algorithm guarantees that the reconstructed fine-scale velocity field is conservative, which makes it suitable to be used to solve the transport problems.

Jenny et al. [11,12] apply the MSFV method to incompressible multiphase flow. In this case, pressure and transport equations are tightly coupled through the total mobility, λ, which is a function of the saturations. To avoid a computationally expensive recalculation of the basis functions, an adaptivity criterion based on total mobility changes was introduced. Once the pressure field is computed, the phase-transport problems are solved on the fine grid. This original version of the MSFV algorithm can be summarized by the following steps:

(1) Given the fine grid on a domain Ω, a conforming coarse grid with M nodes and N cells is constructed. Each coarse cell, $\bar{\Omega}_{i \in [1,N]}$, is composed of multiple fine cells.
(2) A dual coarse grid, conforming to the fine grid, is constructed such that each dual coarse cell, $\tilde{\Omega}^{e \in [1,M]}$, contains exactly one node of the coarse grid in its interior. The dual coarse grid has N nodes, $x_{i \in [1,N]}$, exactly one in the interior of each coarse cell (Fig. 1).
(3) For each dual coarse cell, $\tilde{\Omega}^e$, a set of dual basis functions, $\tilde{\Theta}_i^e$, is constructed; one dual basis function for each node x_i of the dual cell, $\tilde{\Omega}^e$. For each dual basis function an elliptic problem is solved on $\tilde{\Omega}^e$.
(4) For each coarse cell, $\bar{\Omega}_k$, a set of velocity basis functions, $\bar{\Theta}_{ki}$, is constructed, one velocity basis function for each node x_i of the dual cells for which $\bar{\Omega}_k \cap \tilde{\Omega}^e \neq \emptyset$. For each velocity basis function an elliptic problem is solved on $\bar{\Omega}_k$.
(5) The effective transmissibilities of the coarse grid are extracted from the dual basis functions, $\tilde{\Theta}_i^e$.
(6) The coarse-scale transmissibilities are used to compute the coarse-scale pressure values, $\bar{p}_i$, located at the points x_i.
(7) A fine-scale pressure field, $\tilde{p}$, is reconstructed in each coarse cell, $\bar{\Omega}_k$, by superimposing the velocity basis functions multiplied by the corresponding coarse-scale pressure value, i.e. $\tilde{p} = \sum_i \bar{p}_i \bar{\Theta}_{ki}$. The resulting fine scale velocity is conservative at the fine-scale.
(8) The fine-scale velocity field is used to solve the phase transport equations on the fine grid using a fractional flow formulation. To avoid severe time step size restrictions, an implicit scheme can be employed locally on each coarse domain. Global coupling is then achieved by a Schwarz overlap technique.
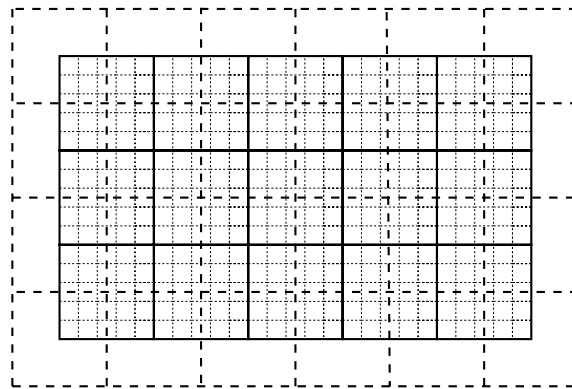(9) If the saturation solution converges, we go directly to step 12.

Fig. 1. Two-dimensional fine grid (thin dotted line) with the imposed coarse grid (bold solid lines) and the corresponding dual coarse grid (bold dashed lines).

(10) Changes of λ require that basis functions are recalculated, which can be done locally and adaptively. Thus, steps 3, 4, and 5 are repeated only for those dual cells and coarse cells, in which the variation of λ are larger than a defined tolerance.

(11) Steps 6–10 are repeated.

(12) The next time step is performed by repeating steps 3–11.

Note that this algorithm consists of two parts. The first part provides effective transmissibilities to compute the coarse-scale pressure. In the second part, a conservative fine-scale velocity field is reconstructed, which allows solving the system of phase transport equations on the fine grid.

This algorithm has the disadvantage of introducing a set of velocity basis functions which are computationally expensive. In this paper we propose a modification of the above algorithm in order to eliminate the second set of basis functions. The new algorithm has the advantage of being much more efficient in most applications and makes it easier to incorporate additional physical processes. The main structure of the algorithm remains unchanged. Modifications concern only step 4, which is suppressed, and step 7, which now reads

(7a) A fine-scale pressure field, $\tilde{p}$, is reconstructed in the computational domain, Ω, by superimposing the dual basis functions multiplied by the corresponding coarse-scale pressure value, i.e. $\tilde{p} = \sum_e \sum_i \bar{p}_i \Theta_i^e$.

(7b) From the pressure field $\tilde{p}$, the fluxes across the coarse-cell boundaries, $\partial\bar{\Omega}_i$, are extracted and used as Neumann boundary conditions to solve the pressure problem in each coarse cell, $\bar{\Omega}_i$. The computed fine-scale velocity field is conservative.

Even if we reconstruct the velocity field in each coarse block at each iteration, in most cases this modified algorithm is more efficient than the algorithm proposed by Jenny et al. [11,12]. Indeed, in the MSFV method the basis functions have to be typically recomputed in 10–30% of the coarse cells [12]. If the velocity basis functions have to be updated in a corse cell, nine local problems have to be solved in two dimensions. Thus, assuming that the velocity basis functions are updated in 20% of the coarse cells at each time step implies that $0.2 \times 9 \times N \approx 1.8 \times N$ local problems have to be solved. In three dimension, the number of coarse-cell problems to be solved increases to $0.2 \times 27 \times N \approx 5.4 \times N$. On the other hand, only N problems have to be solved for the velocity reconstruction with the modified version of MSFV algorithm. Some numerical tests have been performed to estimated the efficiency of the new algorithm in terms of CPU time for incompressible flow problems in 2D heterogeneous media. In our implementation of the MSFV algorithm, the CPU time spent to reconstruct the velocity field with the original algorithm was 1.4–2.2 times larger than the time needed by the new algorithm.

The new MSFV algorithm is not only more efficient, but also more flexible. Indeed, as we will see in the following for the case of compressible flow, additional physical processes can be easily included without affecting the dual basis functions when velocity is reconstructed. From now on we employ only one set of basis functions, therefore we will refer to the dual basis functions simply as "basis functions".

4. Multiscale finite-volume method for compressible multiphase flow

The main challenge with the extension of the above algorithm to compressible flow is to keep the coarse-scale transmissibilities independent of the pressure. Pressure-dependence in the basis functions might require frequent updates, resulting in major loss of attractiveness of the method. The major concern is to avoid this loss of efficiency and keep the solution accurate at the same time. Of course one could introduce an adaptivity criterion and update the basis functions selectively when the pressure change exceed a given threshold. However, as we show in this paper, in the framework of the MSFV method it is possible to obtain accurate results while keeping the basis functions independent of the pressure. Compressibility effects are then taken into account in the coarse problem and, if necessary, in the reconstruction of fine-scale velocity and fluxes. This is made possible by the modified MSFV algorithm proposed in this paper, which does not employ velocity basis functions.

The theoretical justification for this approach relies on the assumption that the last three terms on the r.h.s. of Eq. (4) are small, i.e. temporal and spatial variations of b_α and ϕ within a dual coarse cell are negligible.

These are good approximations for slightly and moderately compressible flows. Note that the time derivative and gradient in the last two terms of Eq. (4) involve $\ln b_\alpha$, which displays much smoother variations than b_α itself. Of course, b_α and ϕ may vary significantly over the whole domain and the coarse pressure equation has to account for compressibility.

In Fig. 2 a coarse outline of the MSFV algorithm for compressible flow is given. Each time step n includes three loops. The coupling loop consists of several iterations to couple the nonlinear pressure equation with the system of nonlinear phase-transport equations. Each iteration, ν_c, of the coupling loop consists of a pressure loop and a saturation loop. At each iteration of these loops linearized equations are solved and convergence is achieved by the Newton–Raphson method. First, the linearized pressure equation is solved implicitly by the MSFV method at each iteration, ν_p, of the pressure loop, then the linearized system of transport equations is solved implicitly inside each coarse cell $\bar{\Omega}_k$ at each iteration, ν_s, of the saturation loop. Coupling is achieved by an overlap between adjacent coarse cells, i.e. the local boundary conditions are defined by the values in the neighbor cells and are updated at each saturation iteration. If necessary to achieve stability in the saturation loop, under-relaxation of the variable is employed. The whole algorithm is sequentially implicit in p and S_α. If needed, the coupling between the pressure and the saturation equations may be increased by reducing to one the maximum number of iterations of the pressure and the saturation loop.

In the following we will explain the steps of the algorithm outlined in Fig. 2 in more detail. The basis functions are exactly the same as for incompressible flow and are updated selectively according to a criterion based on total-mobility change. For completeness, we explain how the basis functions are calculated. Extraction of coarse-scale transmissibilities from the basis functions is analogous to the incompressible-flow case, but now

PSEUDO CODE	EQS.

/* START OF SIMULATION */
 n=1
 do
    /* LOOP I: TIME STEPS */
    $\nu_c = 1$: $S_\alpha^{\nu_c} = S_\alpha^n$, $p^{\nu_c} = p^n$
    do
       /* LOOP II: COUPLING ITERATIONS */
       compute (update) basis functions
       extract coarse-scale transmissiblities
       $\nu_p = 1$: $p^{\nu_p} = p^{\nu_c}$
       do
          /* LOOP III: PRESSURE ITERATIONS */
          solve linearized pressure equation
          $\Rightarrow p^{\nu_p+1}$
          $\nu_p = \nu_p + 1$
       until (convergence of nonlinear pressure equation)
       $p^{\nu_c+1} = p^{\nu_p}$
       construct conservative fine-scale fluxes
       $\nu_s = 1$: $S_\alpha^{\nu_s} = S_\alpha^{\nu_c}$
       do
          /* LOOP IV: SATURATION ITERATIONS */
          solve linearized phase-transport equations
          $\Rightarrow S_\alpha^{\nu_s+1}$
          $\nu_s = \nu_s + 1$
       until (convergence of nonlinear transport equations)
       $S_\alpha^{\nu_c+1} = S_\alpha^{\nu_s}$
       $\nu_c = \nu_c + 1$
    until (convergence of system of pressure and transport equations)
    $p^{n+1} = p^{\nu_c}, S_\alpha^{n+1} = S_\alpha^{\nu_c}$
    $n = n + 1$
 until (simulation done)
	
	 (6)-(8)
	 (11)-(10)
	
	 (13)-(16)
	
	 (18)-(21)
	
	 (30)-(32)

Fig. 2. The MSFV algorithm for compressible flow.

the transmissibilities of each α-phase are considered separately. The coarse-scale pressure equation, together with the reconstruction of the fine-scale fluxes, represents the core of the MSFV method for compressible flow. Special attention is paid to the consistent computation of coarse-scale pressure and fine-scale fluxes, which have to be conservative. Different approximations are considered to compute the accumulation term and the fluxes for the coarse-scale pressure equation and to reconstruct the fine-scale fluxes. Finally, the discretization of the saturation equations is presented.

4.1. Basis functions and effective coarse-scale transmissibilities

According to the definitions given in steps 1 and 2 of Section 3, a coarse grid and a dual coarse grid are imposed. In each dual coarse cell, $\tilde{\Omega}^e$, a set of basis functions, $\tilde{\Theta}_i^e$, is constructed; one basis function for each corner x_i of the dual cell. For Cartesian grids we have 2^d basis functions per dual cell, where d is the number of dimensions. Each basis function is the local numerical solution of the elliptic equation

$$\nabla \cdot (\boldsymbol{\lambda} \cdot \nabla \tilde{\Theta}_i^e) = 0 \quad \text{in } \tilde{\Omega}^e. \tag{6}$$

Boundary conditions are given at the corners x_k by

$$\tilde{\Theta}_i^e(\mathbf{x}_k) = \delta_{ik}, \tag{7}$$

and at the faces $\partial \tilde{\Omega}^e \setminus \{x_k\}$ by

$$\nabla_\perp \cdot (\boldsymbol{\lambda} \cdot \nabla \tilde{\Theta}_i^e)_\perp = 0, \tag{8}$$

where the subscript $\perp$ denotes the vector component normal to $\partial \tilde{\Omega}^e$. Eq. (8) is a closure approximation to localize the problem and in the incompressible case it is the only modeling assumption.

A 3^d-point stencil is used to write the mass-balance equation for the coarse cells and solve the coarse-scale pressure equation. Analogously to the incompressible case, effective transmissibilities are extracted from the basis functions $\tilde{\Theta}_k^e$, but now also b_α has to be taken into account. The contribution of a pressure signal of strength one at node x_k to the α-phase flux in $\tilde{\Omega}^e$ is defined as

$$\boldsymbol{T}_{\alpha k}^e = -b_\alpha f_\alpha \boldsymbol{\lambda} \cdot \nabla \tilde{\Theta}_k^e, \tag{9}$$

where

$$f_\alpha = \frac{k_{r\alpha}/\mu_\alpha}{\sum_{\beta=1}^m k_{r\beta}/\mu_\beta} \tag{10}$$

is the fractional flow of the α-phase. Thus, given the interface between two coarse cells, $\partial \bar{\Omega}_{ij} = \partial \bar{\Omega}_i \cap \partial \bar{\Omega}_j$, we define the transmissibility pertinent to the node x_k as

$$[T_{\alpha k}]_{ij} = \sum_{e=1}^{2^d} \int_{\partial \bar{\Omega}_{ij} \cap \tilde{\Omega}^e} \boldsymbol{T}_{\alpha k}^e \cdot \boldsymbol{\eta} \, d\Gamma, \tag{11}$$

where $\boldsymbol{\eta}$ is the unit vector normal to $\partial \bar{\Omega}_{ij}$ and directed from $\bar{\Omega}_i$ to $\bar{\Omega}_j$. Note that transmissibilities are antisymmetric with respect to the indices i and j, i.e. $[T_{\alpha k}]_{ij} = -[T_{\alpha k}]_{ji}$. Eq. (11) defines the flux across $\partial \bar{\Omega}_{ij}$ extracted from all basis functions defined in dual cells that are adjacent to the node x_k and intersect the interface. It represents the contribution to the flow across the interface for a single pressure signal of strength one applied at the node x_k.

4.2. Coarse-scale pressure equation

A convenient discrete form of Eq. (4) can be obtained by considering the time-implicit discrete formulation of Eq. (1)

$$V_i \frac{\langle \phi^{n+1} b_\alpha^{n+1} S_\alpha^{n+1} \rangle_i - \langle \phi^n b_\alpha^n S_\alpha^n \rangle_i}{\Delta t} + \sum_{k=1}^N \sum_{j=1}^N [T_{\alpha k}^{n+1}]_{ij} \bar{p}_k^{n+1} = -V_i \langle b_\alpha^{n+1} q_\alpha^{n+1} \rangle_i, \tag{12}$$

where $\alpha = 1, \ldots, m$ and $i = 1, \ldots, N$. The old and new time steps are denoted by the superscript n and $n + 1$, respectively, Δt is the time increment, $V_i = \int_{\bar{\Omega}_i} dV$ is the volume of the coarse cell $\bar{\Omega}_i$, and $\langle \ \rangle_i = \frac{1}{V_i} \int_{\bar{\Omega}_i} dV$. Eq. (12) is the mass balance equation for the α-phase in the coarse cell $\bar{\Omega}_i$ and the transmissibility $[T_{\alpha k}]_{ij}$ transforms the pressure signal $\bar{p}_k$ at the node $\boldsymbol{x}_k$ into its contribution to the α-flux across the boundary $\partial \bar{\Omega}_{ij}$. Eq. (12) are linearized around $\bar{p}_k^{v_p} \approx \bar{p}_k^{n+1}$ with $S_\alpha^{n+1} = S_\alpha^{v_c}$, divided by $\langle b_\alpha^{v_p} \rangle_i$, and added. In the following, to simplify the notation, we replace the iteration superscripts v_c and v_p by v, as it is clear from the context and from the coarse outline of the MSFV algorithm in Fig. 2 to which loop the superscript refers. The resulting linearized system of N equations for the coarse-scale pressure is

$$\sum_{k=1}^{N} \left[\frac{V_i}{\Delta t} C_i \delta_{ik} + A_{ik} \right] \bar{p}_k^{v+1} = \frac{V_i}{\Delta t} [C_i \bar{p}_i^v + Q_i], \tag{13}$$

in which the ith equation represents the mass-balance equation for the coarse cell i. In Eq. (13) we have introduced the coefficients

$$C_i = \sum_{\alpha=1}^{m} \frac{\left\langle b_\alpha^v S_\alpha^v \frac{\partial \phi}{\partial p} \Big|^v \right\rangle_i + \left\langle \phi^v S_\alpha^v \frac{\partial b_\alpha}{\partial p} \Big|^v \right\rangle_i + \Delta t \left\langle q_\alpha^v \frac{\partial b_\alpha}{\partial p} \Big|^v \right\rangle_i}{\langle b_\alpha^v \rangle_i}, \tag{14}$$

$$Q_i = \sum_{\alpha=1}^{m} \frac{\left\langle \phi^n b_\alpha^n S_\alpha^n \right\rangle_i - \left\langle \phi^v b_\alpha^v S_\alpha^v \right\rangle_i - \Delta t \langle b_\alpha^v q_\alpha^v \rangle_i}{\langle b_\alpha^v \rangle_i}, \tag{15}$$

and the matrix

$$A_{ik} = \sum_{\alpha=1}^{m} \sum_{j=1}^{N} \frac{[T_{\alpha k}^v]_{ij}}{\langle b_\alpha^v \rangle_i}. \tag{16}$$

The accumulation term Q_i includes both the source terms and the effects of compressibility, and the coefficient C_i contains the derivatives of the pressure-dependent quantities arising from linearization of Q_i. In each step of LOOP III (Fig. 2) the pressure at the new iteration level, $\bar{p}_k^{v_p+1}$, is obtained by multiplying the r.h.s of Eq. (13) by the inverse of the differential operator on the l.h.s. When coarse-scale pressure converges and LOOP III terminates, then $C_i = 0$. For the quantities in brackets, which have to be evaluated inside the coarse cells and at their interfaces, different approximations will be considered. These approximations, which will be discussed in Section 4.4, must be fully consistent with the flux reconstruction in order to guarantee mass-conservation.

4.3. Conservative fine-scale fluxes

After the coarse-scale pressure has been computed, a fine-scale pressure field can be reconstructed by super-imposing the basis functions multiplied by the corresponding coarse pressure values, i.e.

$$\tilde{p}^v = \sum_{e=1}^{M} \sum_{k=1}^{N} \bar{p}_k^v \tilde{\Theta}_k^e. \tag{17}$$

This pressure field cannot be used directly to compute the fine-scale fluxes because the latter would lead to severe mass-balance errors at the dual-cell interfaces [10]. However, $\tilde{p}^v$ can be used to extract the boundary conditions to solve a parabolic problem in each coarse cell and compute fine-scale fluxes. If accumulation term and boundary conditions are defied consistently with the coarse-pressure problem, the resulting fluxes are locally conservative.

Given a coarse cell $\bar{\Omega}_i$ we numerically compute the local fine-scale pressure as the solution of the equation

$$\sum_{\alpha=1}^{m} \frac{1}{\langle b_\alpha^v \rangle_i} \nabla \cdot (b_\alpha^v f_\alpha^v \boldsymbol{\lambda}^v \cdot \nabla p^v) = \frac{Q}{\Delta t} \tag{18}$$

with the boundary conditions

$$(b_\alpha^v f_\alpha^v \boldsymbol{\lambda}^v \cdot \nabla p^v) \cdot \boldsymbol{\eta} = -\sum_{k=1}^{N} \boldsymbol{T}_{\alpha k}^{ev} \bar{p}_k^v \cdot \boldsymbol{\eta} \quad \text{at } \partial \bar{\Omega}_i \cap \tilde{\Omega}^e \tag{19}$$

for each phase $\alpha = 1, \ldots, m$ and the accumulation term defined as

$$Q = \sum_{\alpha=1}^{m} \frac{\phi^n b_\alpha^n S_\alpha^n - \phi^v b_\alpha^v S_\alpha^v - \Delta t b_\alpha^v q_\alpha^v}{\langle b_\alpha^v \rangle_i}. \tag{20}$$

From the fine-scale pressure, p^v, the fine-scale fluxes,

$$\boldsymbol{F} = \begin{cases} -\sum\limits_{\alpha=1}^{m} (b_\alpha^v f_\alpha^v) \boldsymbol{\lambda}^v \cdot \nabla p^v & \text{in } \bar{\Omega}_i, \\ \sum\limits_{\alpha=1}^{m} \sum\limits_{k=1}^{N} \boldsymbol{T}_{\alpha k}^{ev} \bar{p}_k^v & \text{at } \partial\bar{\Omega}_i \cap \tilde{\Omega}^e \end{cases} \tag{21}$$

can be obtained and used to solve the $m - 1$ transport equations.

4.4. Three models to obtain consistent fine-scale fluxes

To ensure conservative fine-scale fluxes it is important that coarse-scale pressure and fine-scale fluxes are computed consistently. That means that, in order to avoid mass-balance errors, the coarse-scale flux across each face $\partial\bar{\Omega}_{ij}$ has to be equal to the integral of the fine-scale fluxes across the same face, i.e.

$$\sum_{k=1}^{N} [T_{\alpha k}^v]_{ij} \bar{p}_k = \sum_{k=1}^{N} \sum_{e=1}^{M} \int_{\partial\bar{\Omega}_{ij} \cap \tilde{\Omega}^e} \boldsymbol{T}_{\alpha k}^{ev} \bar{p}_k \cdot \boldsymbol{\eta} \, \mathrm{d}\Gamma, \tag{22}$$

and that the coarse-scale accumulation term has to be equal to the integral of the fine-scale accumulation terms over the coarse block $\bar{\Omega}_i$, i.e.

$$V_i Q_i = \int_{\bar{\Omega}_i} Q \, \mathrm{d}V. \tag{23}$$

It is straightforward to see that Eq. (22) is automatically satisfied by imposing Eq. (19) as boundary conditions at $\partial\bar{\Omega}_{ij}$, and Eq. (23) by the definition of the coarse scale accumulation term given in Eq. (15). Thus, it is guaranteed by construction that the fine-scale fluxes are conservative. In the following we introduce three models that rely on different assumptions for b_α and ϕ to compute fluxes and accumulation terms.

4.4.1. Piece-wise constant b_α and ϕ (PWC)
The first model assumes that b_α and ϕ can be approximated by piecewise constant distributions, this means that variations of these quantities over distances of the order of the coarse-cell size can be neglected (constant within a coarse cell). Thus, we assume that

$$b_\alpha \simeq \bar{b}_{\alpha i} = b_\alpha(\bar{p}_i) \quad \text{in } \bar{\Omega}_i \tag{24}$$

and

$$\phi_i \simeq \bar{\phi}_i = \phi(\bar{p}_i) \quad \text{in } \bar{\Omega}_i. \tag{25}$$

This model is completely justified for slightly compressible fluids and porous media and it is consistent with the calculation of coarse-scale transmissibilities, which also neglects variations of b_α and ϕ over distance of the order of the coarse-cell size (constant within a dual coarse cell). This formulation has the numerical advantage that the fine-scale and coarse-scale accumulation terms become independent of S^v, i.e.,

$$Q_i = \bar{Q}_i := -\bar{\phi}_i^v + \bar{\phi}_i^n \sum_{\alpha=1}^{m} \frac{\bar{b}_{\alpha i}^n \langle S_\alpha^n \rangle_i}{\bar{b}_{\alpha i}^v} - \Delta t \sum_{\alpha=1}^{m} \langle q_\alpha^v \rangle_i, \tag{26}$$

and the coefficient C_i can be written as

$$C_i = \bar{C}_i := \left.\frac{\partial \bar{\phi}}{\partial \bar{p}}\right|_i^v + \bar{\phi}_i^v \sum_{\alpha=1}^{m} \frac{\langle S_\alpha^v \rangle_i}{\bar{b}_{\alpha i}^v} \left.\frac{\partial \bar{b}_\alpha}{\partial \bar{p}}\right|_i^v + \Delta t \sum_{\alpha=1}^{m} \frac{\langle q_\alpha^v \rangle_i}{\bar{b}_{\alpha i}^v} \left.\frac{\partial \bar{b}_\alpha}{\partial \bar{p}}\right|_i^v. \tag{27}$$

The term $\boldsymbol{T}_{\alpha k}^{ev}$, which appears in the definition of the coarse-scale transmissibilities, Eq. (11), and in the boundary conditions for reconstruction of the fine-scale fluxes, Eq. (19), is now defined as

$$\boldsymbol{T}_{\alpha k}^{e} = -\frac{\bar{b}_{\alpha i} + \bar{b}_{\alpha j}}{2} f_{\alpha} \boldsymbol{\lambda} \cdot \nabla \tilde{\Theta}_{k}^{e} \quad \text{at } \partial\bar{\Omega}_{ij}. \tag{28}$$

4.4.2. Coarse-scale b_{α} and ϕ in the accumulation term (CSA) and fine-scale b_{α} for the fluxes

To improve the ability of our algorithm to model highly compressible flow we first relax the hypothesis of piecewise constant b_{α} and compute them from the reconstructed fine-scale pressure field. Thus we define

$$b_{\alpha} = b_{\alpha}(\tilde{p}) \tag{29}$$

in Eqs. (11), (18), (19) and (21), whereas piecewise constant b_{α} and ϕ are still used for the accumulation terms. Note that this model retains the numerical advantage that the accumulation term is independent of S^{v}.

4.4.3. Fine-scale b_{α} and ϕ in the accumulation term (FSA) and for fluxes

Finally, to deal with highly transient compressible flow, we relax the hypothesis of piecewise constant b_{α} and ϕ for the accumulation term, such that in Eqs. (15) and (20) we use $b_{\alpha} = b'_{\alpha}(\tilde{p})$ and $\phi = \phi\prime(\tilde{p})$ with the constraints $\langle b'_{\alpha}(\tilde{p}) \rangle = b_{\alpha}(\bar{p})$ and $\langle \phi\prime(\tilde{p}) \rangle = \phi(\bar{p})$.

4.5. Phase-transport equations

After the fine-scale fluxes are reconstructed, the $m - 1$ phase-transport equations can be solved implicitly inside each coarse cell $\bar{\Omega}_{k}$ (LOOP IV). Coupling is achieved by an overlap between adjacent coarse cells. After linearization, the discrete transport equation for the α-phase saturation, S_{α}^{v+1}, becomes

$$\frac{\phi^{v} b_{\alpha}^{v}}{\Delta t} S_{\alpha}^{v+1} = -D\left(S_{\beta}^{v+1} - S_{\beta}^{v} \right) - \nabla \cdot f'_{\alpha} \boldsymbol{F} + \frac{\phi^{n} b_{\alpha}^{n} S_{\alpha}^{n}}{\Delta t} - b_{\alpha}^{v} q_{\alpha}^{v}, \tag{30}$$

where

$$D = \sum_{\beta=1}^{m-1} \left[\nabla \cdot \left. \frac{\partial f'_{\alpha}}{\partial S_{\beta}} \right|^{v} \boldsymbol{F} + b_{\alpha}^{v} \left. \frac{\partial q_{\alpha}}{\partial S_{\beta}} \right|^{v} \right] \tag{31}$$

and

$$f'_{\alpha} = \frac{b_{\alpha}^{v} k_{\alpha}^{v} / \mu_{\alpha}}{\sum_{\beta=1}^{m} b_{\beta}^{v} k_{\beta}^{v} / \mu_{\beta}}. \tag{32}$$

To guarantee mass conservation it is important that pressure-dependent variables, i.e. b_{α} and ϕ, are defined consistently with the pressure equation, i.e. according to the same model.

5. Numerical experiments

The extension of the MSFV method to compressible multiphase flow is based on the assumption that the basis functions can be kept independent of the pressure and that they can be computed exactly as for the incompressible case. Rigorously, this assumption is only justified for a slightly compressible flow for which the effects of compressibility can be neglected over a length scale of the order of the coarse cell size. In this case, the last three terms on the r.h.s. of Eq. (4) are approximately zero within a coarse cell (or a dual cell) and the PWC model is a natural choice. In this section we show that pressure-independent basis functions also permit an accurate description of highly compressible flow. In this case, the accuracy of the solution can be improved by using the CSA or the FSA model.

Since we neglect heat transfer and assume constant temperature, the compressibility of the flow can be simply characterized by the isothermal compressibility coefficients of the fluids,

$$c_\alpha = -\frac{1}{V}\frac{\partial V}{\partial p}\bigg|_T = \frac{1}{b_\alpha}\frac{\partial b_\alpha}{\partial p}\bigg|_T \qquad (33)$$

and by the rock compressibility

$$c_R = -\frac{1}{\phi}\frac{\partial \phi}{\partial p}. \qquad (34)$$

The compressibility coefficients of rocks and liquids are typically of the order of 10^{-9}. This means, for instance, that the volume of a liquid, resp. the porosity of a medium, at atmospheric pressure, decreases only by 1% if the pressure is increased by a factor of 100 (i.e. to 10 MPa). Gases are far more compressible. The isothermal gas compressibility coefficients, c_α, at atmospheric pressure are of the order of 10^{-5}. Thus, it is sufficient to double the pressure (i.e. to apply a pressure of about 200 kPa) to reduce the volume of a gas by a factor of 2.

In the following, the porous matrix and the liquid phases will be treated as incompressible and only the compressibility of the gas phase will be taken into account. This assumption is well justified by the large differences among the compressibility coefficients. It is evident that if the MSFV method is able to model a compressible gas phase, even more so it is able to model slightly compressible liquids and rocks. The gas compressibility coefficients cannot be considered constant, but vary with the pressure. We assume that the gas phase behaves like an ideal gas. The isothermal compressibility coefficient of an ideal gas is proportional to the inverse of the pressure, i.e. $c_\alpha \approx 1/p$, which results in the well-known linear relationship between the density and the pressure,

$$b_\alpha = \frac{b_{\alpha 0}}{p_0}p, \qquad (35)$$

where $b_{\alpha 0} = b_\alpha(p_0)$. Table 1 illustrates the physical properties of the fluids considered in the numerical simulations.

In the numerical experiments we consider transport of a tracer in a gas flow, imbibition and drainage of a partially saturated reservoir, depletion of a gas–liquid reservoir and water-flooding of an oil–gas reservoir. In order to separate the inaccuracy introduced by the compressibility models from the inaccuracy introduced by the MSFV algorithm, we first assess and discuss the performance of the three compressibility models proposed in Section 4.4 for 1D homogeneous media. Then, the application to more realistic highly heterogeneous 2D media is presented. The 1D horizontal domain of size L consists of 100 fine cells that have the same permeability. Dirichlet boundary conditions are imposed at the two ends of the computational domain. The coarse grid used in the MSFV method consists of five cells, which corresponds to an upscaling factor of 20. The permeability of the 2D horizontal domain of size $L_x \times L_y$ is represented on a fine 220×60 grid. It is the same as the top layer of the second model of the 10th SPE Comparative Solution Project (SPE 10) [5], which was designed as a benchmark for different upscaling techniques. This layer belongs to a Tarabert formation with isotropic horizontal permeability that varies over six orders of magnitude. The variance of the log-permeability is $\sigma_{\ln k}^2 = 5.49$ and the coefficient of variation is CV = 2.97 (Fig. 3). The coarse grid used in the MSFV method consists of 22×6 cells, which corresponds to an upscaling factor of 10×10. At the long sides no-flow boundary conditions are imposed, while constant-pressure boundary conditions are imposed at the short sides.

The MSFV solution is compared with a reference solution obtained by solving a fine-scale problem. The overall solution algorithm is sequentially implicit in p and S_α. For the fine-scale solution, an upwind scheme

Table 1
Properties of the fluids used in the numerical simulations

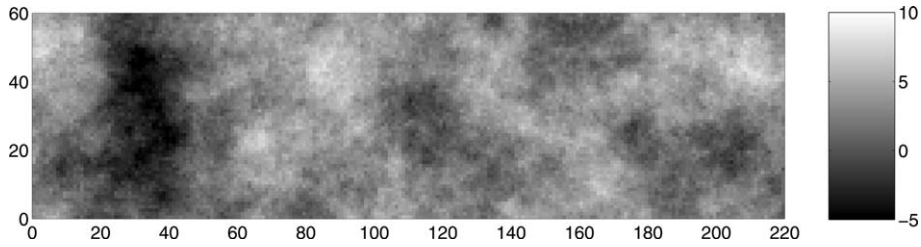| Fluid	Viscosity μ (Pa s)	Density b_0 (kg/m^3)	$1/p_0$ (Pa^{-1})
Water	10^{-3}	1000	–
Oil	10^{-2}	900	–
Air	1.8×10^{-5}	1.20	10^{-5}
Methane	10^{-5}	0.68	10^{-5}
Carbon dioxide	1.4×10^{-5}	2.81	10^{-5}

Fig. 3. The natural logarithm of the 2D permeability field; the permeability field is extracted from the top layer of the three-dimensional SPE 10 model; the variance of the log-permeability is $\sigma_{\ln k}^2 = 5.49$, which corresponds to a coefficient of variation CV = 2.97.

is used for the relative permeabilities, whereas a central scheme is used for b_α. In the MSFV method, the same discretization scheme is employed to solve the local problems for the flux reconstruction, whereas a central scheme for the total mobility is used to compute the basis functions in order to keep them independent of pressure distribution.

5.1. Tracer transport in gas

First we consider the case in which the 1D homogeneous reservoir is initially saturated with air and at atmospheric pressure (0.1 MPa). At the left boundary an ideal tracer is injected at constant concentration c_0 and at a constant pressure of 1 MPa. The pressure at the right boundary is kept constant at 0.1 MPa. Note that, according to the ideal gas law, the air density varies by a factor of 10 over the whole domain. This problem can be modeled by treating the pure gas and the gas with tracer as separated phases with linear relative permeabilities. In this framework, the saturation represent the concentration of the tracer normalized by the injection concentration, i.e. $S = c/c_0$. Dispersion is not modeled explicitly and only numerical dispersion is present.

In Fig. 4 the normalized concentration, $S = c/c_0$, at four different dimensionless times $t/\tau = 2.5 \times 10^{-3}$, 2.5×10^{-2}, 1.25×10^{-1} and 2.5×10^{-1} is plotted, where $\tau = \mu \phi L^2/k\Delta p$, $\mu = \mu_{air}$ and Δp is the applied pressure difference between the left and the right boundaries. At early time (e.g. $t/\tau = 2.5 \times 10^{-3}$), differences between the MSFV solutions and the fine-scale reference solution are observed. These are due to the fact that elliptic pressure equations are solved in the dual coarse cells, which results in a faster propagation of the reconstructed
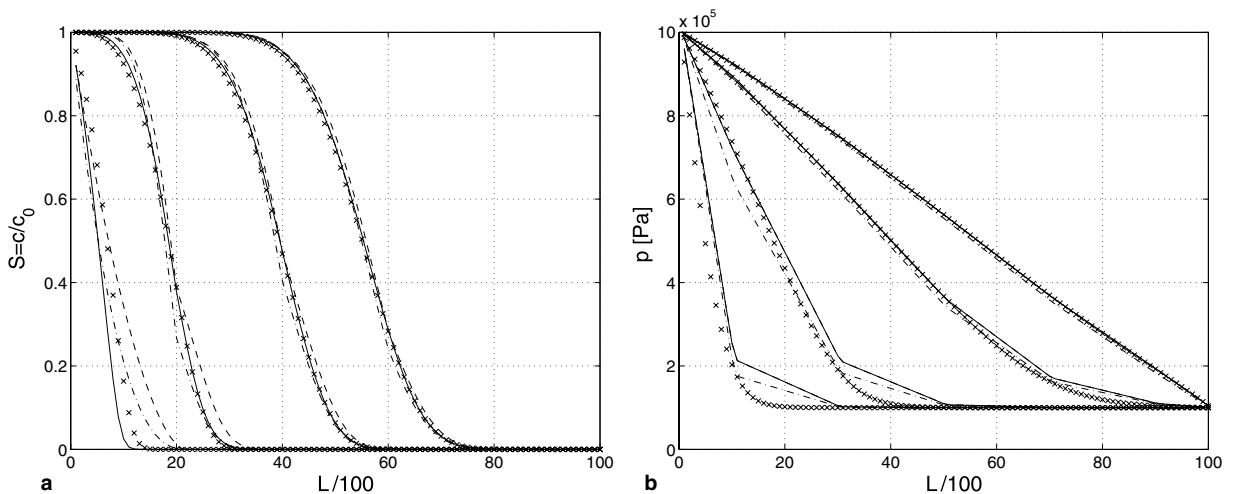

Fig. 4. One-dimensional tracer transport in gas; normalized tracer concentration, $S = c/c_0$, (a) and pressure (b) at dimensionless times $t/\tau = 2.5 \times 10^{-3}$, 2.5×10^{-2}, 1.25×10^{-1} and 2.5×10^{-1} ($\tau = \mu_{air}\phi L^2/k\Delta p$) for the fine-scale reference solution (crosses), the PWC model (dot-dashed line), the CSA model (dashed line), and the FSA model (solid line); the upscaling factor is 20 and flow is from left to right.

pressure signal (Eq. (17)) compared with the reference-pressure signal, which is the solution of a parabolic equation (Fig. 4). Indeed, if the coarse pressure $\bar{p}$ changes at one node of the dual grid, the reconstructed pressure field $\tilde{p}$ immediately changes in all adjacent dual cells. This effect has a larger impact on the saturation solutions if the accumulation term is computed with constant $b = b(\bar{p})$ within a coarse cell (PWC and CSA models). At later time, however, all three models perform well and are in very good agreement with the reference solution. It is important to notice that discrepancies at early time do not increase, but decrease with time. The reason is that all three models are very accurate in predicting the coarse-scale mass fluxes at coarse-cell interfaces. The deviations from the reference solution observed at early time are due to the flux-reconstruction procedure, which is inaccurate if the curvature of the pressure profile is large, but does not affect the coarse-scale mass balance. In general, we can say that, even though differences are minor, the FSA model provides the most accurate saturation solution and the PWC model the most accurate pressure solution.

We now consider an analogous numerical experiment in the 2D heterogeneous reservoir described earlier (Fig. 3). As in the 1D test case, the reservoir is initially saturated with air and the pressure is 0.1 MPa. Constant pressure boundary conditions are imposed at the left and right boundaries (10 MPa and 0.1 MPa, respectively) and an ideal tracer at constant concentration c_0 is injected at the left boundary. Linear relative permeabilities are employed for both phases. Note that a factor of 100 variation of air density corresponds to the applied pressure difference. The MSFV solutions are in good agreement with the fine-scale reference solution as can be seen in Fig. 5, where the maps of the normalized-concentration, $S = c/c_0$, at $t/\tau = 5.7 \times 10^{-1}$ are compared. The time scale τ is defined by $\tau = \mu \phi L_x^2 / \exp(\langle \ln k \rangle) \Delta p$, where L_x is the length of the reservoir and μ is the viscosity of the injected fluid. This result shows the robustness and accuracy of the three compressibility models, which provide accurate solutions for problems with extreme density variations within a single coarse cell. Indeed, in the test case considered, a pressure drop of about 8 MPa takes place in the low-permeability region between $x = 20$ and $x = 40$ (Fig. 3). This corresponds to a density variation by a factor of 40 within a coarse cell. The accuracy of the MSFV solutions can be expressed in terms of the L^1-errors,

$$\epsilon(S) = \frac{\|S - S^{\text{ref}}\|_1}{\|S^{\text{ref}} - S_0\|_1}, \tag{36}$$

where $S_0 = S(t^* = 0)$ is the initial condition (Table 2), and by drawing the isoline of $S - S^{\text{ref}}$ (Fig. 6). The most accurate solutions are obtained with the CSA and FSA models.

5.2. Imbibition and drainage of a partially saturated reservoir

In this section we study the displacement of a phase by another phase that has a different compressibility. Since the two phases are immiscible, the relative permeabilities are modeled as quadratic functions of the saturation. Note that in the case of imbibition in a gas-saturated reservoir, the effects of compressibility are almost negligible. Indeed, due to the large difference in viscosity between gas and water, the pressure drop mainly takes place in the water phase and the very small pressure gradient in the gas phase does not allow large density variations. Thus, as a more challenging test case, we consider the injection of a mixture consisting of 90% water and 10% air in a reservoir that initially contains 10% of water and 90% of air. The initial pressure in the reservoir is 0.1 MPa. Dirichlet conditions are applied at the western and eastern boundaries (1 MPa and 0.1 MPa, respectively). This corresponds to a factor of 9 variation of air density.

The CSA and the FSA models give excellent results for the 1D homogeneous reservoir (Fig. 7). In contrast, the PWC solution deviates from the reference and shows a stepwise behavior. Due to the assumption of piecewise constant b, air density is discontinuous at coarse-cell interfaces and this results in saturation jumps. Moreover, the amount of water in the reservoir is larger and the water front travels faster than in the reference solution (Fig. 7). This excess of water is accumulated at early times (i.e. $t/\tau < 2.25 \times 10^{-3}$) and stops increasing at late times.

The simulations performed in the 2D heterogeneous domain, performed with $\Delta p = 1$ MPa, confirm the results of the 1D simulations (Figs. 8 and 9). The PWC model predicts an excess of water in the reservoir, a wetting front that travels slightly faster than the reference-solution front, and saturation jumps between
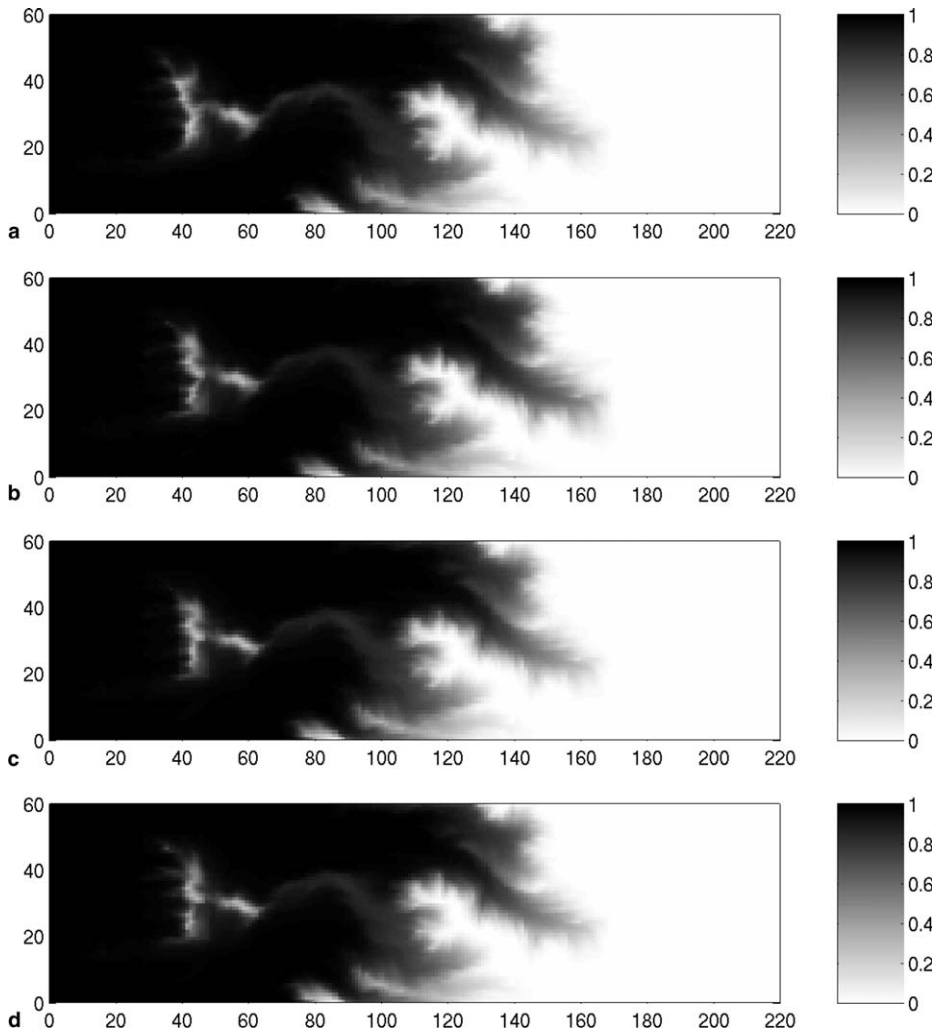
Fig. 5. Two-dimensional tracer transport in gas; normalized tracer concentration, $S = c/c_0$, at dimensionless times $t/\tau = 5.7 \times 10^{-1}$ ($\tau = \mu_{air} \phi L_x^2 / \exp(\langle \ln k \rangle) \Delta p$) for the fine-scale reference solution (a), the PWC model (b), the CSA model (c), and the FSA model (d); the upscaling factor is 10×10.

Table 2
L^1 errors of the 2D saturation fields ($\epsilon(S) = \|S - S^{ref}\|_1 / \|S_{ref} - S_0\|_1$) for the three compressibility models; the upscaling factor is 10×10

Problem	Δp (MPa)	t^* [−]	$\epsilon(S)$			Figure
			PWC	CSA	FSA	
Gas tracer test	10	5.7×10^{-3}	9.0×10^{-2}	8.2×10^{-2}	5.3×10^{-2}	
Gas tracer test	10	5.7×10^{-2}	6.6×10^{-2}	5.1×10^{-2}	4.9×10^{-2}	
Gas tracer test	10	5.7×10^{-1}	3.9×10^{-2}	2.5×10^{-2}	2.5×10^{-2}	5, 6
Imbibition	1	3.1×10^{-1}	2.9×10^{-2}	2.1×10^{-2}	2.2×10^{-2}	8, 9
Imbibition	1	3.1	4.1×10^{-2}	1.3×10^{-2}	1.3×10^{-2}	8, 9
Depletion	1	2.9×10^{-3}	4.8×10^{-1}	3.8×10^{-1}	3.9×10^{-1}	12
Depletion	1	2.9×10^{-2}	3.6×10^{-1}	2.1×10^{-1}	2.1×10^{-1}	
Depletion	1	2.9×10^{-1}	2.2×10^{-1}	9.2×10^{-2}	8.9×10^{-2}	12

coarse cells in the low-permeability region between $x = 20$ and $x = 40$, where the pressure drop is about 0.9 MPa. The solutions obtained with the CSA and FSA models are very accurate and almost identical (see also Table 2).
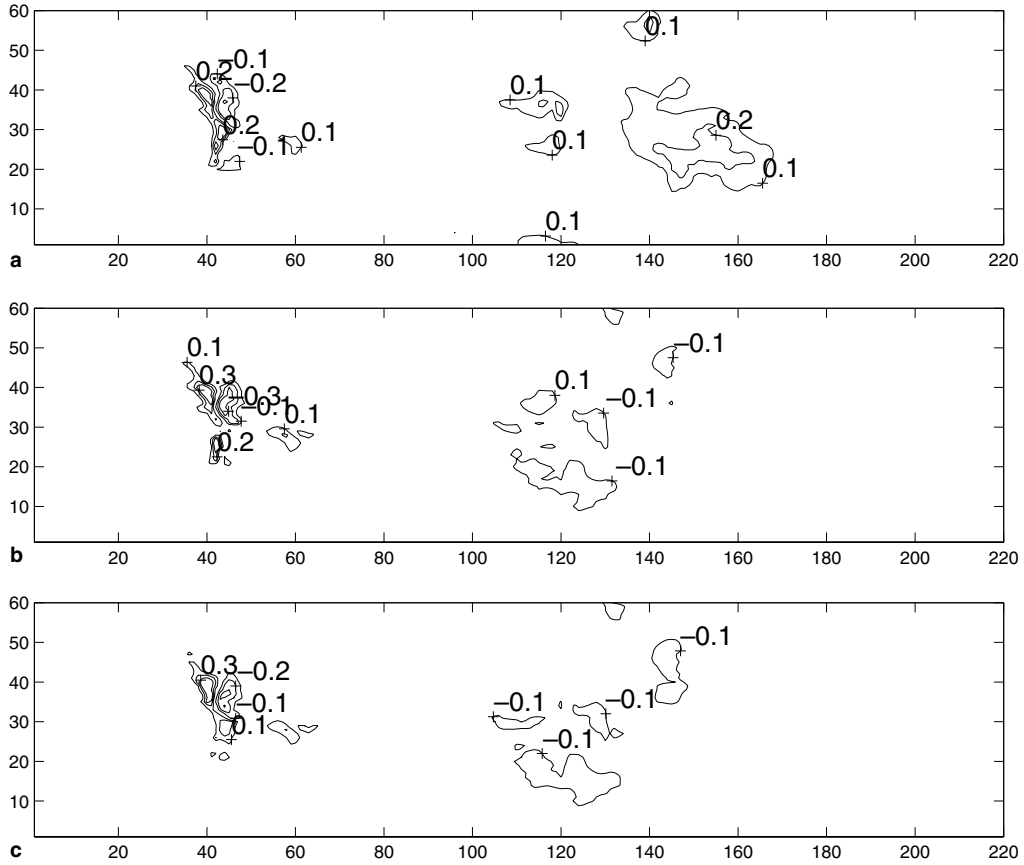
Fig. 6. Two-dimensional tracer transport in gas; normalized tracer-concentration error, $S - S^{\text{ref}}$, at dimensionless times $t/\tau = 5.710^{-1}$ ($\tau = \mu_{\text{air}} \phi L_x^2 / \exp(\langle \ln k \rangle) \Delta p$) for the PWC model (a), the CSA model (b), and the FSA model (c); isolines are drown at $S - S^{\text{ref}} = -0.3, -0.2, -0.1, 0.1, 0.2, 0.3$; the upscaling factor is 10×10.
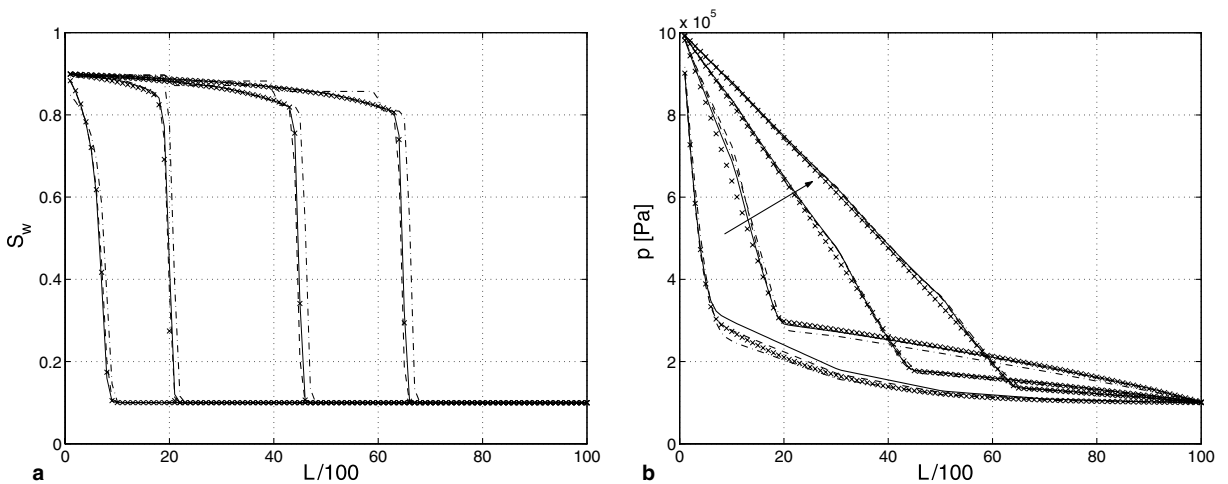

Fig. 7. One-dimensional imbibition problem; water saturation (a) and pressure (b) at dimensionless times $t/\tau = 2.25 \times 10^{-3}$, 2.25×10^{-2}, 1.13×10^{-1} and 2.25×10^{-1} ($\tau = \mu_w \phi L^2 / k \Delta p$) for the fine-scale reference solution (crosses), the PWC model (dot-dashed line), the CSA model (dashed line), and the FSA model (solid line); flow is from left to right and the arrow indicates the temporal evolution of the pressure profiles.
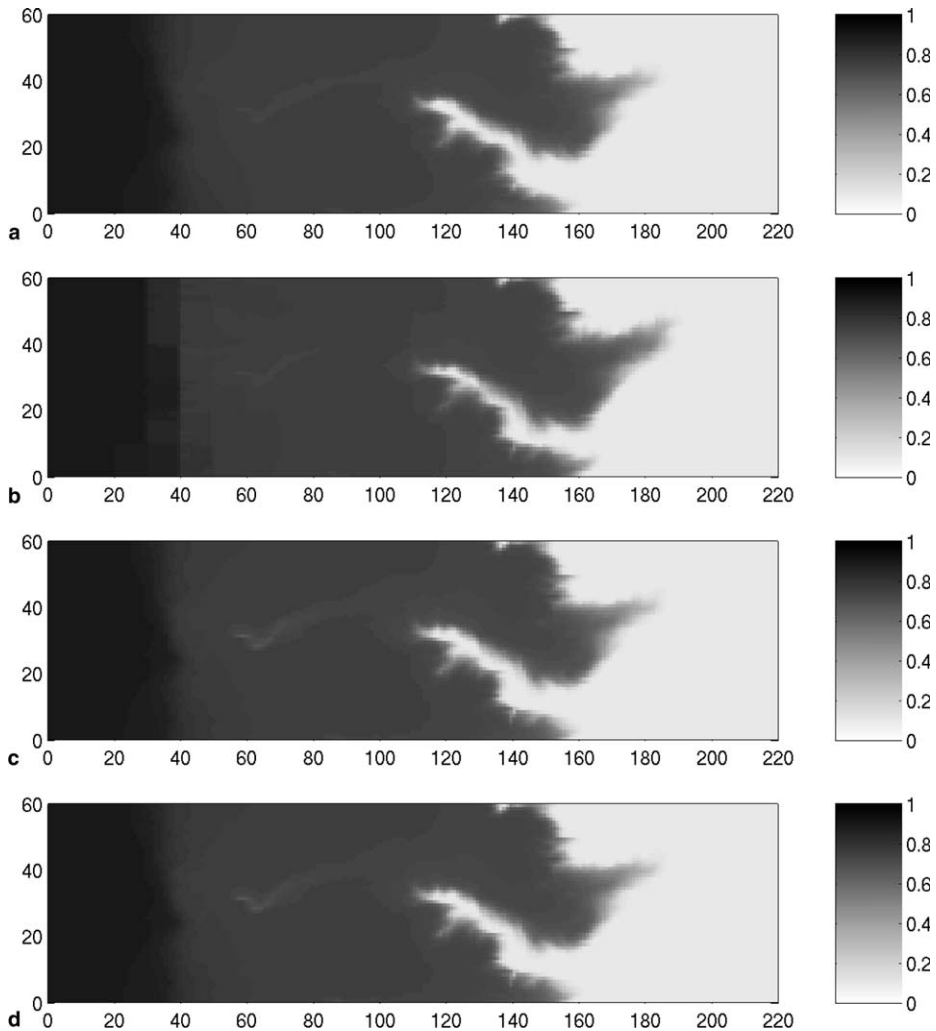
Fig. 8. Two-dimensional imbibition problem; water saturation at dimensionless times $t/\tau = 3.1$ ($\tau = \mu_w \phi L_x^2 / \exp(\langle \ln k \rangle)\Delta p$) for the fine-scale reference solution (a), the PWC model (b), the CSA model (c), and the FSA model (d); the upscaling factor is 10×10.

To highlight the differences between the CSA and FSA models we consider a drainage problem in which the accumulation term plays a relevant role. In the reservoir, which initially contains 90% water and 10% air, a mixture of 10% water and 90% is injected from the left. As in the previous test case, the initial pressure is 0.1 MPa and Dirichlet boundary conditions are applied at the left and right boundaries (1 MPa and 0.1 MPa, respectively). The displaced fluid is less mobile and accumulates ahead of the invading front. In this region the pressure increases and air is compressed, which results in a higher water saturation. Fig. 10 shows the solution of the 1D homogeneous problem at time $t/\tau = 0.25$. Whereas the result obtained with the FSA model is still accurate, the solutions obtained with the other two models exhibit a stepwise water-saturation profile. This is due to the fact that in the CSA and PWC models constant air density is assumed in each coarse cell for the accumulation term. According to these models, air is uniformly compressed within a coarse cell, which is not a good approximation in the region ahead of the invading front.

5.3. Depletion of a liquid–gas reservoir

As an ultimate test for the compressibility models, we considered the depletion of a liquid–gas reservoir. The reservoir is initially at a pressure of 1 MPa and contains 50% water and 50% air. The relative permeabilities are
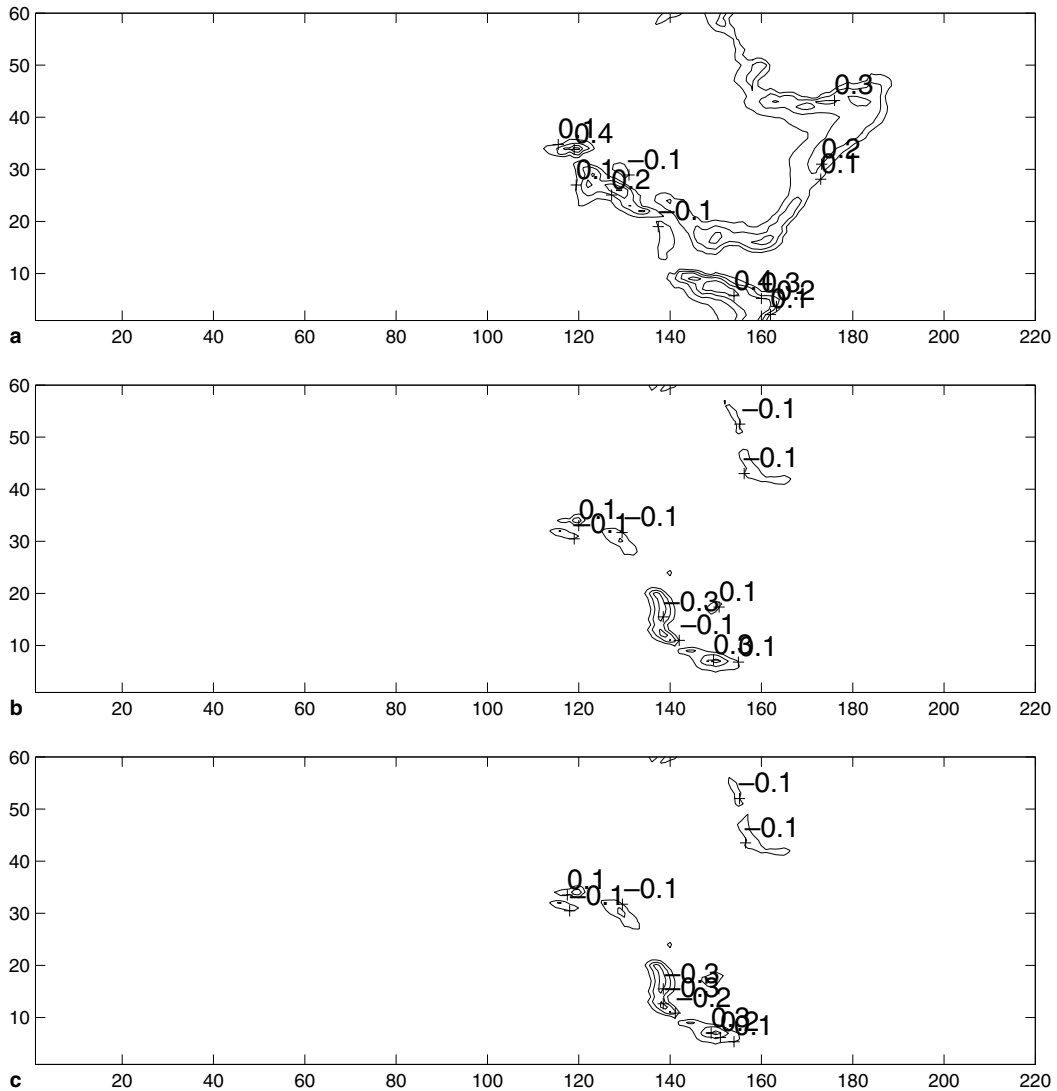
Fig. 9. Two-dimensional imbibition problem; water-saturation error, $S_w - S_w^{\mathrm{ref}}$, at dimensionless times $t/\tau = 3.1$ ($\tau = \mu_w \phi L_x^2 / \exp(\langle \ln k \rangle) \Delta p$) for the PWC model (a), the CSA model (b), and the FSA model (c), isolines are drown at $S - S^{\mathrm{ref}} = -0.3, -0.2, -0.1, 0.1, 0.2, 0.3$; the upscaling factor is 10×10.

modeled as quadratic functions. At time zero the right boundary is opened and brought to a pressure of 0.1 MPa. The left boundary is kept at a pressure of 1 MPa with $S_w = 0.5$. When the pressure drops, air expands and the saturation in the reservoir changes. Note that the saturation distribution is compressibility driven in the sense that it only depends on the compressibility ratio of the two fluids and would remain equal to the initial saturation if the two fluids had the same compressibility.

The distributions of water-saturation and pressure for the 1D homogeneous test case are shown in Fig. 11, which clearly show that the PWC model fails to predict the correct saturation profile. At early times, the saturation distribution is non-monotonic and the saturation gradient in the coarse cells is reversed compared to the reference solution. This can be intuitively explained by the fact that in the reference solution the mass flux increases going from left to right, even though the air density decreases. The density decrease partially compensates the effects of the increasing pressure gradient and relative permeability, and reduces the growth of air-mass flux. Since in the PWC the fine scale fluxes are reconstructed neglecting compressibility within coarse cells, the air flux tends to be underestimated in the left and overestimated in the right part of the cell,
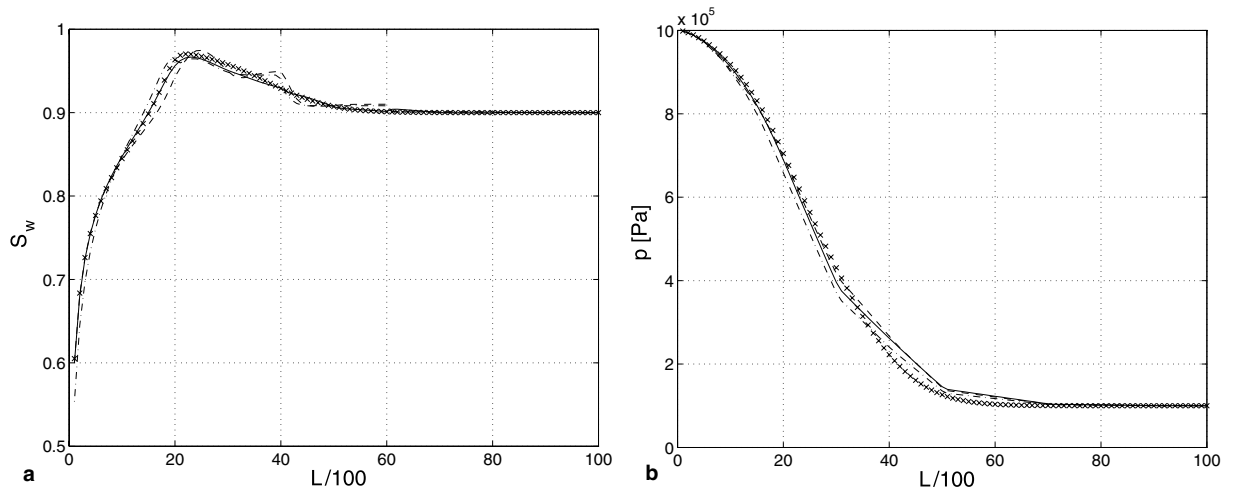
Fig. 10. One-dimensional drainage problem; water-saturation (a) and pressure (b) at dimensionless time $t/\tau = 2.5 \times 10^{-1}$ ($\tau = \mu_{\text{air}}\phi L^2/k\Delta p$) for the fine-scale reference solution (crosses), the PWC model (dot-dashed line), the CSA model (dashed line), and the FSA model (solid line); flow is from left to right.
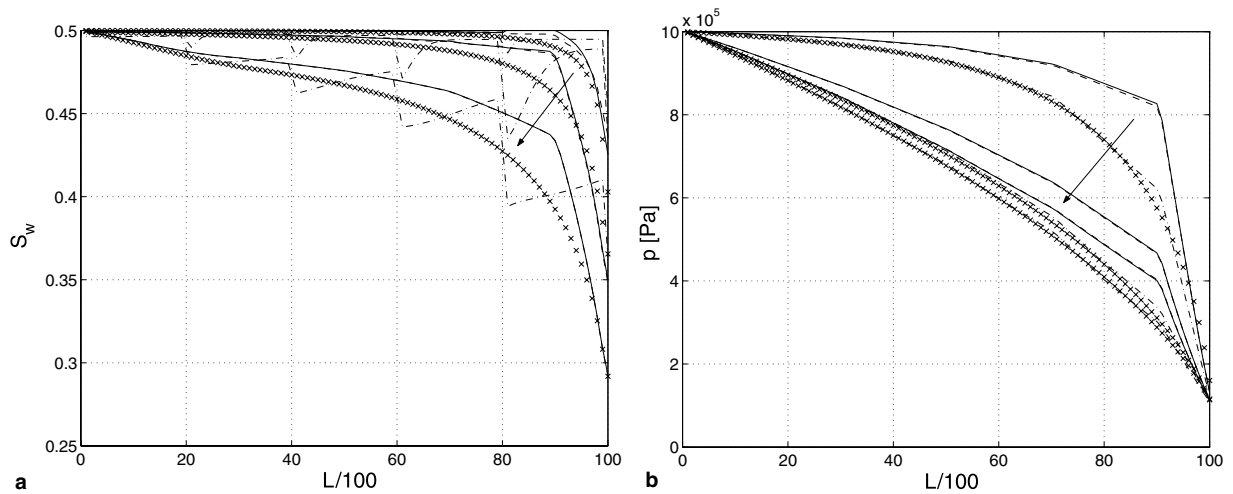

Fig. 11. One-dimensional depletion problem; water-saturation (a) and pressure (b) at dimensionless times $t/\tau = 0.14$, 1.4, and 14 ($\tau = \mu_{\text{air}}\phi L^2/k\Delta p$) for the fine-scale reference solution (crosses), the PWC model (dot-dashed line), the CSA model (dashed line), and the FSA model (solid line); the arrows indicate the temporal evolution of the profiles.

which results in a local water-phase accumulation at the right coarse-cell boundary. In a sense, the decrease of air saturation going from left to right yields a decrease of relative permeability, which takes the place of air-density decrease in reducing the growth of the air-mass flux. Note, however, that the reconstructed pressure, $\tilde{p}$, is in excellent agreement with the reference solution.

The saturation solutions obtained with the CSA and FSA models are more accurate. However, they also deviate from the reference solution, e.g. there is a slower drop of the water saturation and a very pronounced knee located at the center of the eastern coarse cell. Since in the MSFV method the fine-scale pressure $\tilde{p}$ is reconstructed by a linear combination of the basis functions, which are obtained neglecting compressibility and solving elliptic problems, the maximum pressure gradient, $\nabla\tilde{p}$, is limited and $\tilde{p}$ is unable to capture strong curvatures. Note that this is less critical for the PWC model since the smaller pressure gradient is compensated by a larger b_α. If the saturation distribution is completely determined by the pressure trough the compressibility
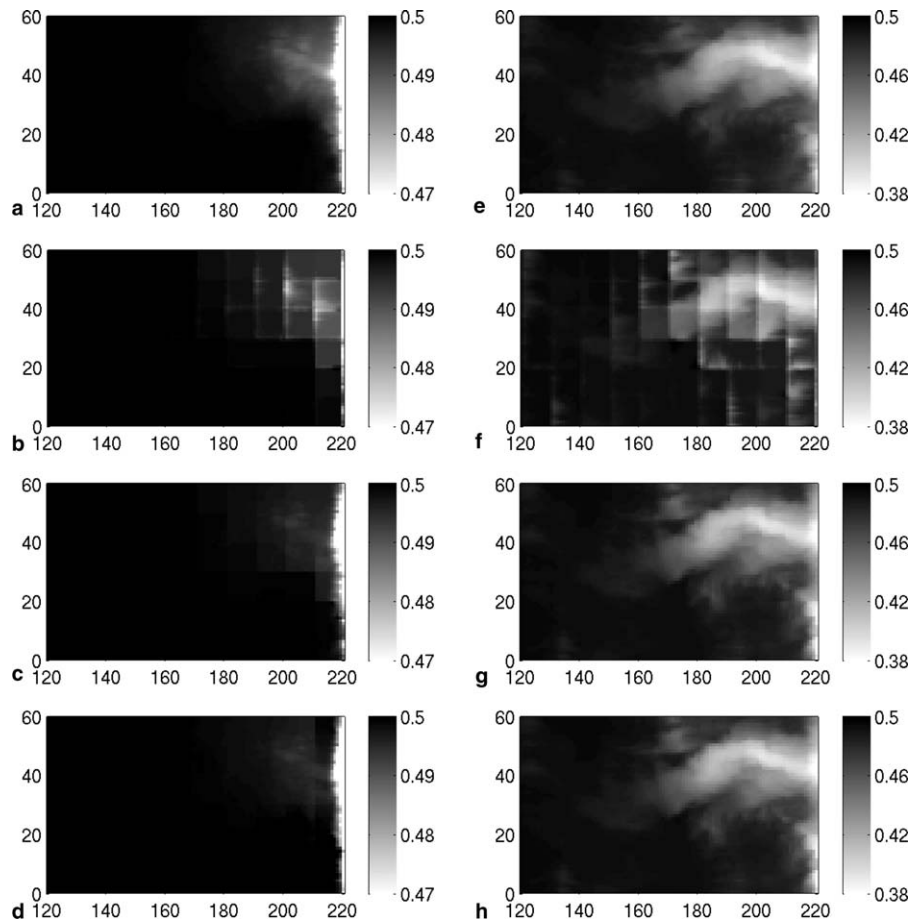
Fig. 12. Two-dimensional depletion problem; water saturation at dimensionless times $t/\tau = 2.9 \times 10^{-3}$ (left) and $t/\tau = 0.29$ (right) for the fine-scale reference solution (a,e), the PWC model (b,f), the CSA model (c,g), and the FSA model (d,h); the upscaling factor is 10×10 and $\tau = \mu_{\mathrm{air}} \phi L_x^2 / \exp(\langle \ln k \rangle) \Delta p$; only the right part of the reservoir is shown (i.e. from $x = 120$ to $x = 220$).

coefficient, significant differences between the reference solution and the solutions obtained with the CSA and the FSA models can occur. This problem might be overcome by using the pressure obtained from the flux reconstruction, which includes the effects of compressibility (Eq. (18)), instead of $\tilde{p}$ to compute b_α.

The CSA solution and the FSA solution are very similar and differences can be observed only at very early times when the accumulation terms play a more important role. Note that in the case of liquid and gas (which have very different viscosities) the large mobility of air reduces the impact of the accumulation term: it is more convenient for the air to move rather than getting compressed. At early times, a slight overshoot of the FSA solution can be observed in the most right coarse cell, more precisely between $x = 80$ and $x = 90$. Again, this overshoot is due to the fact that $\tilde{p}$ is obtained from basis functions that are solutions of elliptic problems. When the reservoir is opened, the average accumulation in the right coarse cell is close to zero, but significant deviations from zero occur locally. Therefore, within the coarse cell, the fluids distribute according to the accumulation term.

The solutions of the 2D heterogeneous depletion problem are shown in Fig. 12, where the saturation maps at time $t/\tau = 2.9 \times 10^{-3}$ and $t/\tau = 0.29$ are plotted. Whereas the PWC model fails to predict the correct fine-scale saturation distribution, the CSA and FSA models provide relatively accurate solutions, especially at later times (see also Table 2). At early times, differences between the CSA and FSA models can be observed. In particular, the CSA solution shows small saturation jumps between coarse cells (chessboard-like saturation distribution), which are due to the piecewise constant b used in the accumulation term.
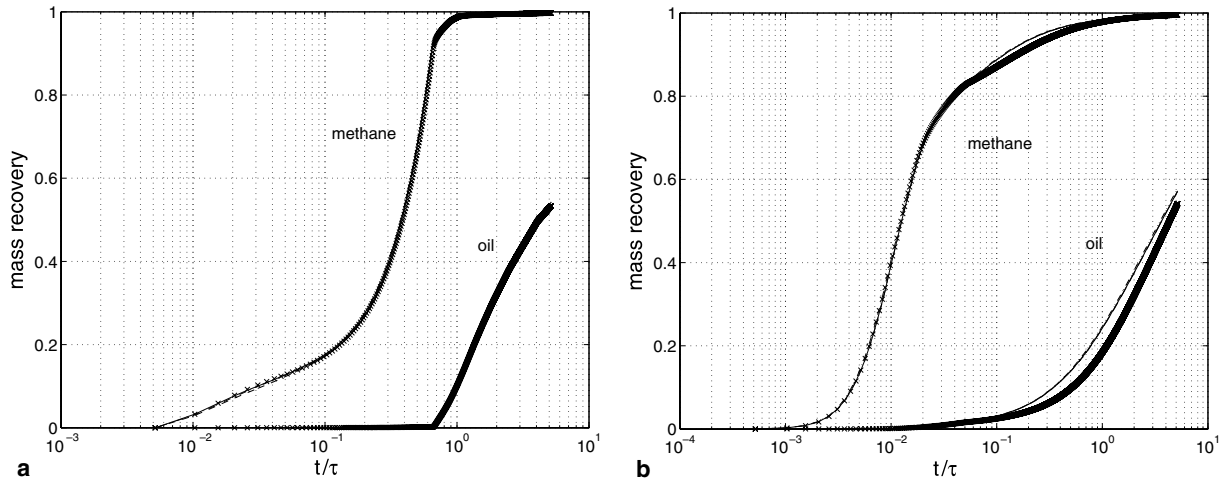
Fig. 13. Two-dimensional flooding problem; methane- and oil-mass recovery as a function of the dimensionless time t/τ ($\tau = \mu_{oil}\phi L_x^2 / \exp(\langle \ln k \rangle)\Delta p$) for the fine-scale reference solution (crosses), the PWC model (dot-dashed line), the CSA model (dashed line), and the FSA model (solid line); both water-flooding (a) and CO_2-flooding (b) are shown.

5.4. Flooding of an oil-gas reservoir

Finally, we briefly demonstrate an application of the MSFV method to three-phase compressible flow in the 2D heterogeneous domain. We consider a reservoir that initially contains 70% oil and 30% methane and is at a pressure of 0.1 MPa. Pressure at the left and right boundaries are set to 1 MPa and 0.1 MPa, respectively. At time zero a third phase is injected at the left boundary; both water and CO_2 injections are considered. For all phases quadratic relative permeability are used. The resulting methane- and oil-recovery curves are shown in Fig. 13. It can be seen that for the water-flooding test case the agreement with the reference curves is excellent. In the case of CO_2-flooding the oil-recovery predicted by the MSFV method is slightly higher.

6. Conclusions

Accurate solutions for a large spectrum of compressible-flow problems can be obtained with the MSFV method without modifying the basis functions that are used to compute the coarse-scale transmissibilities. The basis functions are computed as in the case of incompressible flow and are therefore independent of the pressure. The effects of compressibility are taken into account to solve the coarse-scale pressure equation and, if necessary, to reconstruct the fine-scale fluxes.

Three models with an increasing level of complexity in the flux reconstruction have been tested for multi-phase compressible problems in which at least one phase follows the ideal gas law. The most simple model (PWC model) neglects the effects of compressibility at the fine-scale and treats the flow as compressible only at the coarse scale. This model is justified only for slightly compressible flows in which the typical length of density variations is larger than the coarse-cell size. However, it proved to work also in case of significant density variations within a coarse cell. This demonstrates that this simple model can be successfully used to describe the compressibility of the porous medium and the compressibility of liquids (at isothermal conditions). In regions where large pressure drops occur over a coarse cell, the saturation field predicted by this model is not accurate enough.

More accurate saturation distributions can be obtained with two more sophisticate models that take into account the effects of compressibility in the fine-scale flux reconstruction. These models differ in the way they treat the accumulation term: in one model (CSA model) the accumulation term does not depend on the pressure distribution within the coarse cells, whereas in the other model (FSA model) it does. In most problems they yield almost identical solutions, because the effects of the accumulation term are limited by the large gas to liquid viscosity ratio, and the agreement with the reference saturation solution is excellent. The

most accurate solutions are obtained with an accumulation term that depends on the pressure distribution within the coarse cells.

The most challenging problem is the depletion of a gas-liquid reservoir in which the saturation distribution is purely compressibility-driven. Even though this is an extreme test case, it is of great practical interest, because it describes processes that take place in the vicinity of a well. Also for this test case the agreement between the reference solution and the MSFV solutions is satisfactory, if compressibility is taken into account in the flux reconstruction. If, however, a more accurate prediction of the saturation is needed, the accuracy of the MSFV solutions can be improved by using the pressure from the flux reconstruction to compute the density (in place of the pressure obtained by superimposing the basis functions multiplied by the corresponding coarse-scale pressure). This can implicitly be done by solving fully compressible nonlinear problems for the flux reconstruction in each coarse cell employing Newton–Raphson iterations. Another way to improve the accuracy, specifically around a well, is to include gas compressibility in the well basis function. Indeed, it has been shown by Wolfsteiner et al. [15] that correct modeling of wells in the MSFV method requires an additional basis function that accounts for the additional degree of freedom.

Acknowledgments

References

[1] J.E. Aarnes, V. Kippe, K.A. Lie, Mixed multiscale finite elements and streamline methods for reservoir simulation of large geomodel, Adv. Water Res. 28 (2005) 257–271.

[2] T. Arbogast, Implementation of a locally conservative numerical subgrid upscaling scheme for two phase Darcy flow, Comput. Geosci. 6 (2002) 453–481.

[3] T. Arbogast, S.L. Bryant, A two-scale numerical subgrid technique for waterflood simulations, Soc. Petrol. Eng. J. (2002) 446–457.

[4] Z.M. Chen, T.Y. Hou, A mixed multiscale finite element method for elliptic problems with oscillating coefficients, Math. Comput. 72 (242) (2003) 541–576.

[5] M.A. Christie, M.J. Blunt, Tenth SPE comparative solution project: A comparison of upscaling techniques, SPE 66599, presented at the SPE Symposium on Reservoir Simulation, Houston, February 11–14, 2001.

[6] G. Dagan, Flow and Transport in Porous Formations, Springer-Verlag, New York, 1989.

[7] Y. Gautier, M.J. Blunt, M.A. Christie, Nested girding and streamline-based simulation for fast reservoir performance prediction, Comput. Geosci. 3 (1999) 295–320.

[8] R.J. Hoeksema, P.K. Kitanidis, Analysis of the spatial structure properties of selected aquifers, Water Resour. Res. 21 (4) (1985) 563–572.

[9] T.Y. Hou, X.H. Wu, A multiscale finite element method for elliptic problems in composite materials and porous media, J. Comput. Phys. 134 (1) (1997) 169–189.

[10] P. Jenny, S.H. Lee, H. Tchelepi, Multi-scale finite-volume method for elliptic problems in subsurface flow simulation, J. Comput. Phys. 187 (1) (2003) 47–67.

[11] P. Jenny, S.H. Lee, H. Tchelepi, Adaptive multiscale finite-volume method for multi-phase flow and transport in porous media, Multiscale Model. Simulat. 3 (1) (2004) 50–64.

[12] P. Jenny, S.H. Lee, H. Tchelepi, Fully implicit adaptive multi-scale finite-volume algorithm for multi-phase flow in porous media, J. Comput. Phys., 2006 (submitted for publication).

[13] Ph. Renard, G. de Marsiliy, Calculating equivalent permeability: a review, Water Resour. Res. 20 (5–6) (1997) 253–278.

[14] X.H. Wen, J.J. Gómez-Hernández, Upscaling hydraulic conductivities in heterogeneous media: an overview, J. Hydrol. 183 (1–2) (1996) R9–R32.

[15] C. Wolfsteiner, S.H. Lee, H.A. Tchelepi, Well modeling in the multiscale finite volume method for subsurface flow simulation. Multiscale Model. Simulat., 2006 (submitted for publication).